Detection of microaneurysms using multi-scale correlation coefficients

Bob Zhang [a], Xiangqian Wu [b,c], Jane You [c,*], Qin Li [c], Fakhri Karray [a]

[a] Department of Electrical and Computer Engineering, University of Waterloo, Waterloo, ON, Canada
[b] School of Computer Science and Technology, Harbin Institute of Technology, Harbin, PR China
[c] Biometrics Research Center, Department of Computing, The Hong Kong Polytechnic University, Kowloon, Hong Kong

ARTICLE INFO

ABSTRACT

This paper presents a new approach to the computer aided diagnosis (CAD) of diabetic retinopathy (DR)—a common and severe complication of long-term diabetes which damages the retina and cause blindness. Since microaneurysms are regarded as the first signs of DR, there has been extensive research on effective detection and localization of these abnormalities in retinal images. In contrast to existing algorithms, a new approach based on multi-scale correlation filtering (MSCF) and dynamic thresholding is developed. This consists of two levels, microaneurysm candidate detection (coarse level) and true microaneurysm classification (fine level). The approach was evaluated based on two public datasets—ROC (retinopathy on-line challenge, http://roc.healthcare.uiowa.edu) and DIARETDB1 (standard diabetic retinopathy database, http://www.it.lut.fi/project/imageret/diaretdb1). We conclude our method to be effective and efficient.

© 2010 Elsevier Ltd. All rights reserved.

1. Introduction

Images of the ocular fundus, also known as retina images or retinal (fundus) images, can provide useful information about retinal [1], ophthalmic, and even systemic diseases such as diabetes [2–14], hypertension [15], glaucoma [16,17], obesity arteriosclerosis [18] and retinal artery occlusion. One such condition, diabetic retinopathy (DR), is the result of long-term diabetes and involves the formation on the retina of lesions which can lead to blindness.

In order to prevent the damage of this severe complication to patients' vision, it is very important to diagnose diabetic retinopathy and provide appropriate treatment to minimize further deterioration as early as possible. Since microaneurysms are the first signs of DR, its detection is vital. It is also crucial to monitor the development of the disease and classify changes in retinal images taken at different medical examinations to evaluate the effectiveness of the medical treatment and observe the evolution of DR.

In general, DR can be classified into four stages: mild non-proliferative diabetic retinopathy (NPDR), moderate NPDR, severe NPDR, and proliferative diabetic retinopathy (PDR). The damage caused by DR can be reduced and major vision loss [19,20]

prevented if it is diagnosed and treated in its early stages. Thus, regular examination of diabetic patients' retina is very important. However, it is time consuming and subject to human errors if DR diagnosis is conducted by medical professionals manually. Therefore, automated or computer-aided analysis of diabetic patients' retina can help eye care specialist to screen larger populations of patients more accurately. An image processing approach provides a powerful tool in three aspects: image enhancement and feature extraction (feature based image registration), mass screening (diagnosis) and change detection and classification (monitoring).

Fluorescein angiography (FA) is an imaging technique for evaluation of retinal vascular disease, particularly DR [7–9,14,21]. Fluorescein dye is injected intravenously and the fluorescence within retinal vessels is then photographed through a matched combination of excitation and barrier filters. Although FA produces very clear gray-scale retinal images as seen in Fig. 1(a) and is effective for describing hemorrhages and neovascularization, it is not well-accepted by patients because of its intrusive nature. Therefore, it is essential to develop a safe, fast, easy, and comfortable way to observe and capture the retina. The analysis of color retinal images [3–6,13] seen in Fig. 1(b) (a color fundus image, produced by a fundus camera) is viewed as this feasible approach because the acquisition of color retinal images is non-intrusive, very fast and easy. A fundus camera is essentially a specialized microscope with an attached camera that allows you take photographs of the interior surface of the eye.

Processing of color retinal images is usually conducted in its green channel since microaneurysms have the highest contrast

* Corresponding author. Tel.: +852 2766 7293; fax: +852 2774 0842.
E-mail addresses: yibo@pami.uwaterloo.ca (B. Zhang), xqwu@cs.hit.edu.cn (X. Wu), csyjia@comp.polyu.edu.hk (J. You), csli@comp.polyu.edu.hk (Q. Li), karray@pami.uwaterloo.ca (F. Karray).
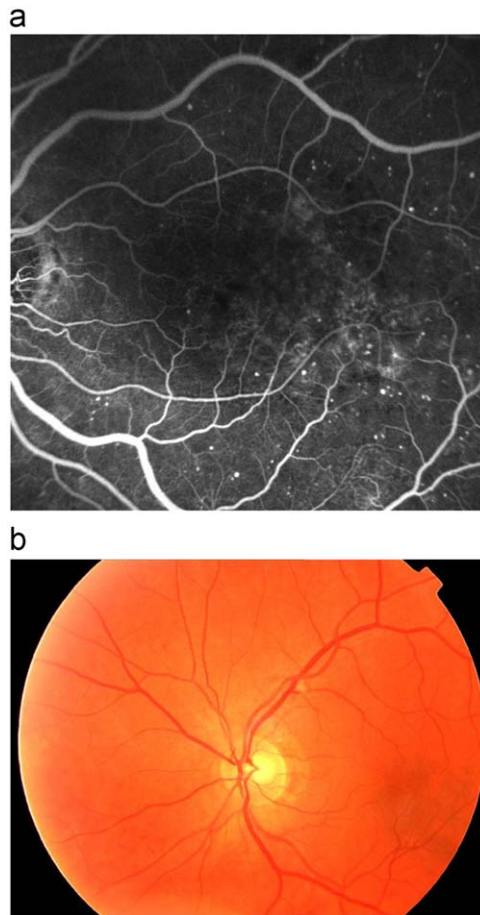
Fig. 1. Most common DR screening techniques: (a) FA (fluorescein angiograms) and (b) color retinal image.

with its background here. This is illustrated in Fig. 2, which represents the image components in three different color bands—Fig. 2(a) is an original color retinal image, Fig. 2(b–d) represents component in red band (I_{red}), green band (I_{green}) and blue band (I_{blue}), respectively. In the green band objects such as blood vessels, microaneurysms, the optic disk, etc., are most visible.

In [11], an artificial neural network (ANN) was used to automatically classify microaneurysms. The ANN consisted of an input pixel layer, hidden layer and output layer, and was trained to recognize features such as blood vessels, exudates and hemorrhages (hemorrhages or microaneurysms). Each image was divided into 30×30 and 20×20 squares pixels depending on the feature being detected and a trained observer then classified the squares as normal retina not showing blood vessels (normal), normal retina showing normal blood vessels (vessel), retina showing exudates (exudates), or retina showing hemorrhages or microaneurysms (hemorrhage). However, this method only classifies the regions of microaneurysms without extraction and localization. In addition, the use of a neural network is time consuming.

It is very difficult to detect microaneurysms by classifying hemorrhages because their pixel values are similar to that of blood vessels. Several approaches have been proposed to tackle this challenge. In [13], a mathematical morphology [14] based method was developed to detect microaneurysms in color retinal images. The proposed algorithm consisted of several stages. In the image preprocessing stage the image background was removed to create a "shade corrected" image. This was accomplished by subtracting the image with the result of a 25×25 median filter applied to the image. Afterwards, candidate extraction was performed on the "shade corrected" image by extracting vessels with morphological opening using 12 rotated linear structuring elements at $15°$ and produced 12 responses. Taking the maximum pixel values of all 12 responses at each pixel location produced a vascular map which was subsequently removed from the "shade
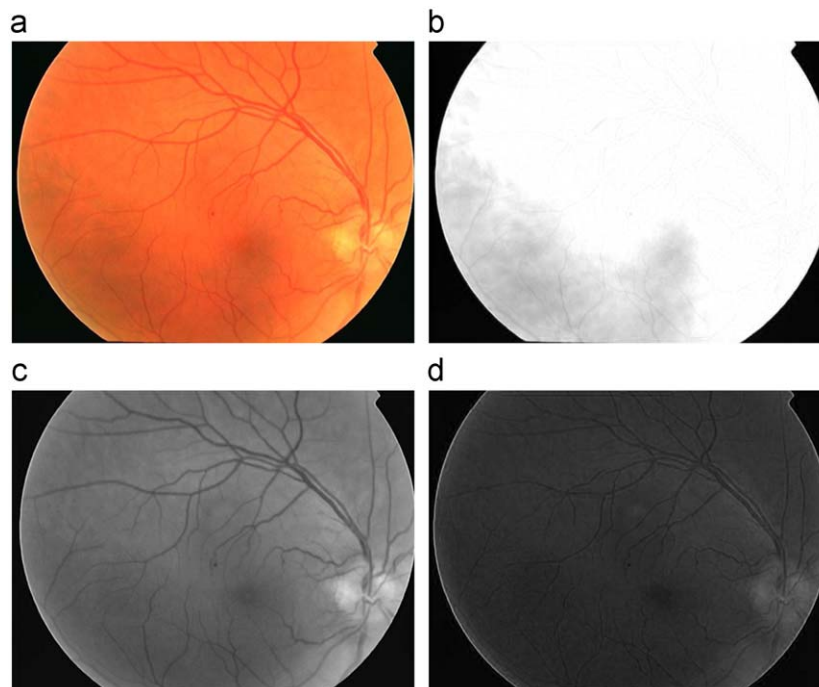
Fig. 2. The corresponding color bands: (a) red, (b) green, and (c) blue of the color retinal image (Fig. 1(b)). (For interpretation of the references to color in this figure legend, the reader is referred to the web version of this article.)
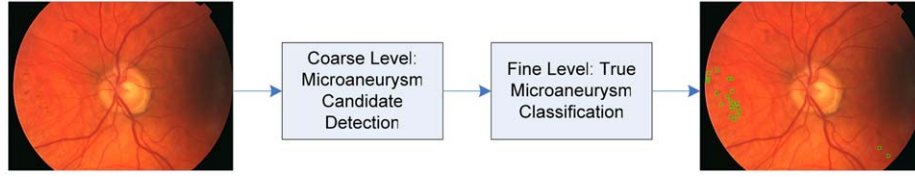
Fig. 3. System architecture of the proposed algorithm.

corrected" image. The remaining candidates inside this image should no longer contain elongated structures but red lesions. Region growing was applied to each candidate before 13 features based on shape and color intensities were extracted. This was used to construct a feature vector for classification. The author also described another way to detect red lesions in fundus images based on the fusion of candidate detection and pixel classification. Initially, all of the lesion candidates were located by combining mathematical morphology [14] with pixel classification, where the pixels were classified using a k-NN classifier with a reference standard that requires manually marking each image pixel. Finally, all of the marked candidates are further classified as red lesion or non-red lesion by a k-NN using additional 68 features extracted from each candidate.

It is noted that pixel classification found in [11,13] involves medical experts labeling each pixel, something not feasible when using greater number of images. When the length of the structuring element [13,14] is increased to be able to detect larger objects, the vessel segmentation deteriorates leading to more spurious candidate objects being detected on the vessel, which limits the effectiveness of the proposed methods.

The algorithm presented in [28] applied wavelet image decomposition. It compared a small window of the image with a microaneurysm template modeled by a Gaussian curve. The comparative result was the squared errors sum between coefficients of each sub-band and the microaneurysm's corresponding coefficients. Thresholds were used to separate microaneurysms from other structures. However, only two scales were used to model microaneurysms, which is not sufficient for real applications.

A three-stage scheme for the detection of microaneurysms was presented in [25]. Firstly, the image was divided into different sub-regions with image enhancement. Secondly, local adaptive thresholding was applied to detect microaneurysms. Thirdly, prior knowledge in the sense that microaneurysms cannot occur on the optical disk, vessels and hard exudates were incorporated for final output. Unfortunately, a comprehensive testing on the proposed algorithm is not reported except the preliminary results on the detection of additional objects such as optical disk and hard exudates in retinal images.

There are many other methods for the detection of microaneurysms. The algorithm presented in [27] can be divided into four steps. The first step consisted of image enhancement: shade correction and image normalization of the green channel. The second step was candidate detection using diameter closing with an automatic threshold scheme. The third step involved feature extraction to facilitate the forth step of classification which was based on kernel density estimation in conjunction with Bayesian risk minimization. However, the diameter closing and thresholding in the second step may cause the loss of important feature points which are crucial for further processing and final classification.

Local contrast normalization with local vessel detection was regarded as another useful approach to detect microaneurysms [26]. After the initial preprocessing stage, a watershed retinal region growing method was applied to be used for contrast normalization of each candidate microaneurysm. Local vessel detection that occur with microaneurysms and a k-NN classifier was used to classify the candidates. Nevertheless, this method is complicated and its results are based on cross-validation of the training set instead of splitting the dataset into training and test.

To avoid the limitations of the above algorithms for better performance, this paper presents a novel approach to the CAD of diabetic retinopathy that applies a hierarchical approach to detect microaneurysms in retinal images. The approach applies multi-scale correlation filtering (MSCF) and dynamic thresholding for intensity-based detection and localization of microaneurysms in retinal images in a two-level hierarchical architecture. In the first level (coarse level), we detect candidate microaneurysms using MSCF. In the second level (fine level), we classify true microaneurysms by extracting 31 features from the level one candidates which are used to classify them. Fig. 3 shows the architecture of the proposed system.

The remainder of this paper is organized as follows. Sections 2 and 3 describe the two level system architectures in detail. Section 4 presents and discusses the experimental results. Section 5 offers our conclusion and an outline of future work.

2. Coarse level: microaneurysm candidate detection

The task for course-level detection is to identify all possible microaneurysm candidates in a retinal image. Fig. 4(a) and (b) shows two microaneurysms that were found in Fig. 1(b) (shown in its green channel) and Fig. 4(c) and (d) shows their corresponding grayscale distributions. As can be seen, microaneurysms exhibit a Gaussian shape. This allows us to use a Gaussian function to detect microaneurysms according to the similarity between the distributions of its grayscale. The Gaussian function can be defined as

$$G(x,y) = \frac{1}{2 \cdot \pi \cdot \sigma^2} \exp\left(\frac{-x^2 + y^2}{2 \cdot \sigma^2}\right) \tag{1}$$

with its distribution shown in Fig. 5.

The correlation coefficient is a good way to measure the resemblance between the Gaussian function and grayscale distribution of microaneurysms. If the two match, the correlation coefficient will be high and if they do not, the value will be low. The range of the coefficient is from 0 to 1.

The correlation function is defined as

$$r = \frac{\sum_m \sum_n (A_{mn} - \overline{A})(B_{mn} - \overline{B})}{\sqrt{\left(\sum_m \sum_n (A_{mn} - \overline{A})^2\right)\left(\sum_m \sum_n (B_{mn} - \overline{B})^2\right)}} \tag{2}$$

where $\overline{A}$ and $\overline{B}$ are the mean.

Since microaneurysms vary in size, different sigma values for the Gaussian kernel are required. For this purpose we include the selection of multiple scales in order to match various microaneurysms dimensions. Fig. 6(a–d) shows the responses and maximum correlation coefficients to different Gaussian kernels of the same two microaneurysms depicted in Fig. 4. Images (a, c) on the left show the responses of Fig. 4(a) to small and large kernels,

a

b

c

d
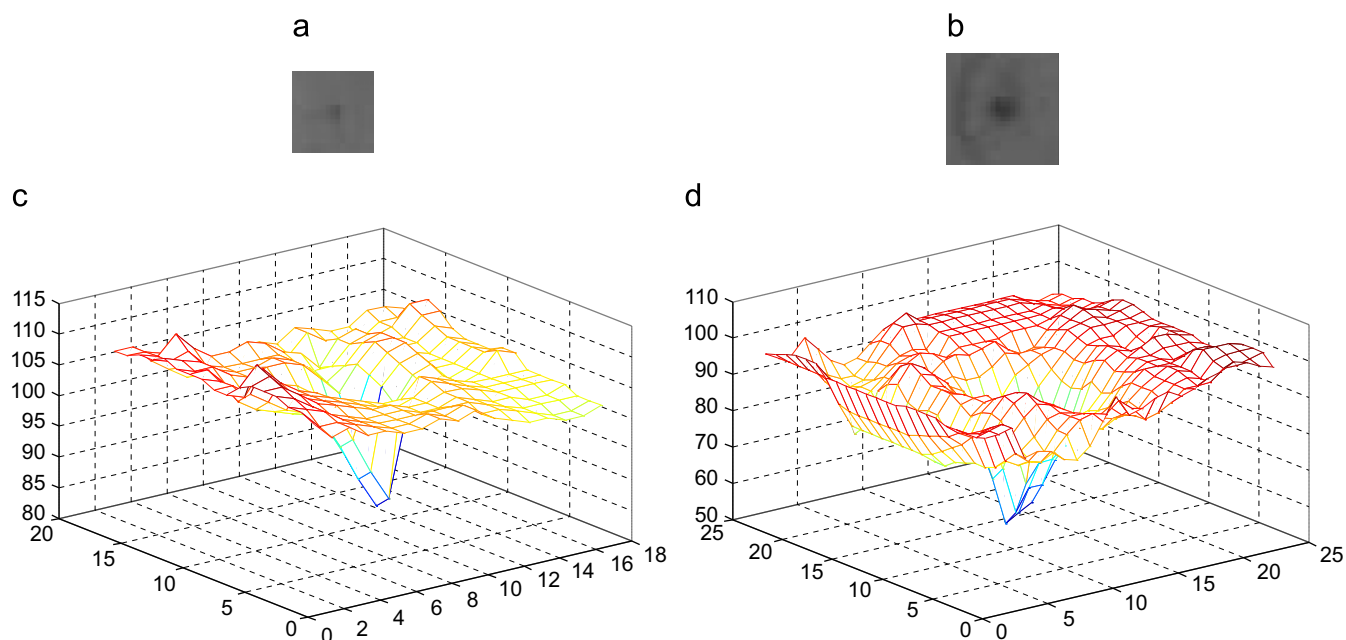
Fig. 4. The detection of microaneurysms in a color retinal image. (a) and (b) illustrate two microaneurysms found in Fig. 2(a). The corresponding mesh plots of (a) and (b) are shown in (c) and (d), respectively. (For interpretation of the references to color in this figure legend, the reader is referred to the web version of this article.)

a

b
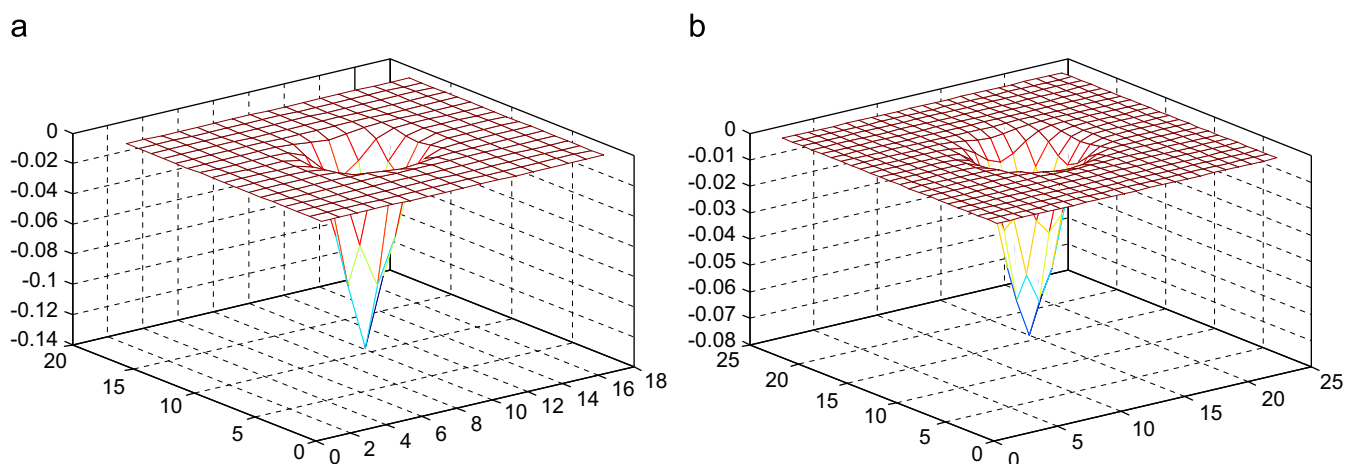
Fig. 5. The mesh plots of the Gaussian kernel with different scale factors: (a) scale factors=1.1 and (b) scale factors=1.5.

respectively. Images (b, d) on the right show the same thing but using Fig. 4(b). From Fig. 6 it can be seen that applying one scale does not guarantee detection of the maximum coefficient as response Fig. 6(a) has a greater coefficient using the smaller scale Gaussian kernel while response Fig. 6(d) produces a higher coefficient using the larger scale kernel.

The first step in coarse level candidate detection involves applying a sliding neighborhood filter with multi-scale Gaussian kernels to the fundus image in order to calculate a correlation coefficient for each pixel.

Because microaneurysms are circular, the Gaussian kernels are also circular as this will ensure that the response (a correlation coefficient) will be high. Based on extensive experimentation, we chose five scales for the kernel to represent microaneurysms of different sizes with the sigma of the Gaussian function being 1.1, 1.2, 1.3, 1.4 and 1.5. The maximum coefficients from each of the five responses were combined to form a final response. Fig. 7

a   b

0.6871   0.5081

c   d

0.4349   0.7458
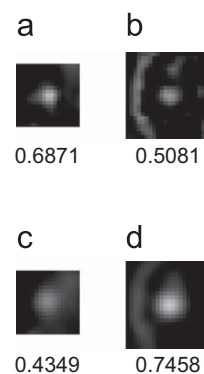
Fig. 6. The responses of lesions to different Gaussian kernels: (a) and (b) are responses for lesions in Fig. 4(a) and (b) at a small scale, (c) and (d) are responses for lesions in Fig. 4(a) and (b) at a larger scale, respectively, where the maximum coefficient is placed below each responses.
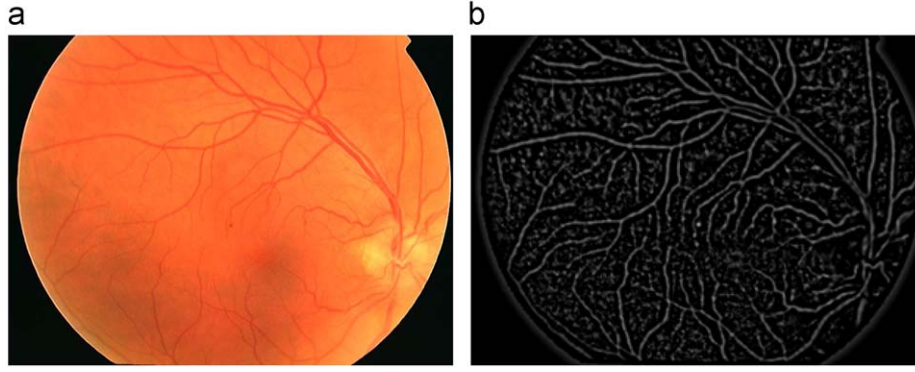
Fig. 7. The final response of a testing image: (a) the input retinal image and (b) the output.
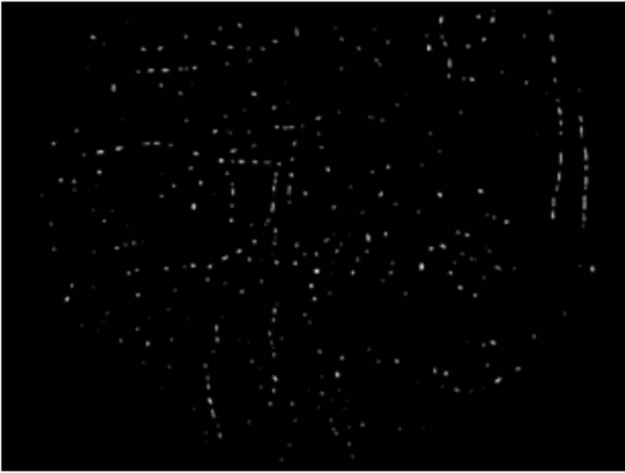

Fig. 8. Result after segmenting Fig. 7 with a threshold of 0.4. The white spots marked are possible microaneurysms.

depicts the final response, where Fig. 7(a) is an input retinal image and Fig. 7(b) is the output. The brighter spots seen in Fig. 7(b) have a higher coefficient and therefore are more likely to be true microaneurysms.

A threshold is next applied in order to determine the number of microaneurysm candidates. Application of a threshold creates a binary image as seen in Fig. 8, where the threshold value was set to 0.4 in order to segment Fig. 7. Since microaneurysms cannot occur on blood vessels, adaptive thresholding [29] was used to first locate these vessels and remove any spots on them, thereby reducing the number of candidates. Fig. 9 shows a vascular map, where Fig. 9(a) is an original image and Fig. 9(b) is the output of the corresponding vascular map with all the blood vessels that were detected after adaptive thresholding. Any candidates on these vessels are removed from Fig. 8 and the result can be seen in Fig. 10.

The candidate microaneurysms that remain in Fig. 10 at this point do not represent the true microaneurysms size; therefore, we apply region growing based on [13]. We first calculate the grayscale intensity pixel value(s) for each candidate (i_{green} for I_{green} and i_{bg} for I_{bg}). I_{bg} is the background of I_{green} and is computed by applying a median filter of size 25×25 to I_{green}. The lowest intensity in i_{green} ($I_{darkest}$) is also required. These values are used to find a threshold t where

$$t = I_{darkest} - x \cdot (I_{darkest} - i_{bg}) \tag{3}$$

In this paper x is set to 0.5. The value t is then used to segment I_{green} into a binary image where region growing begins from the pixel having intensity $I_{darkest}$ and terminates when no more pixels are connected to it. If the resultant region is > 120 pixels it is discarded as no true microaneurysms can be that large. Fig. 11 shows the result of region growing for the candidates in Fig. 10.

3. Fine level: true microaneurysm classification

The task for fine level microaneurysm classification is to detect true microaneurysms in the candidate set, which can be implemented through feature extraction. We used a total of 31 features for each candidate, based on shape, grayscale pixel intensity, color intensity, responses of Gaussian filter-banks, and correlation coefficient values. Table 1 lists the 31 features used to discriminate microaneurysms in our proposed approach. Features 27–29 are unique to the proposed method as it is based on the correlation coefficient of each pixel, calculated beforehand. The last two features, major and minor axis length are added to diversify the already existing shape features.

Some of the features listed above require I_{SC} and I_{match}. Below we describe how they are calculated. I_{SC} is I_{green} with the background removed computed as $I_{green} - I_{bg}$ and can be seen in Fig. 12. Blood vessels in I_{SC} are located with morphological open using 12 line structures of length nine pixels rotated at $15°$. The maximum pixel values after applying the 12 structures show only the blood vessels. These vessels are then subtracted from I_{SC} to form I_{lesion} where linear structures are removed and microaneurysms are kept. To improve the contrast of I_{lesion} in order to make microaneurysms standout from its background, an 11×11 pixels Gaussian filter with $\sigma = 1$ is convoluted with I_{lesion}. The result of which is I_{match} depicted in Fig. 13.

After features are extracted from the candidates, the feature vector is divided into two groups: true microaneurysms and false microaneurysms. The details of the process are summarized in Section 4. The minimum and maximum values of each feature in the true microaneurysms group are obtained and stored in a discrimination table as in Table 2. The 31 features are given a number in the leftmost and the minimum and maximum values for that feature can be read off in the columns. This table can be used to eliminate any candidates whose feature values are greater than maximum or less than minimum. For example, Feature 16 which computes the contrast of the candidates and its surrounding area in the green channel, the minimum value was manually set to 8. By manually setting this value to be higher than the actual minimum of Feature 16, some true and many microaneurysm candidates are removed. This feature was specifically chosen since the contrast between microaneurysms and its surrounding background are known to be high (in the green channel). The remaining candidates whose feature values are between minimum
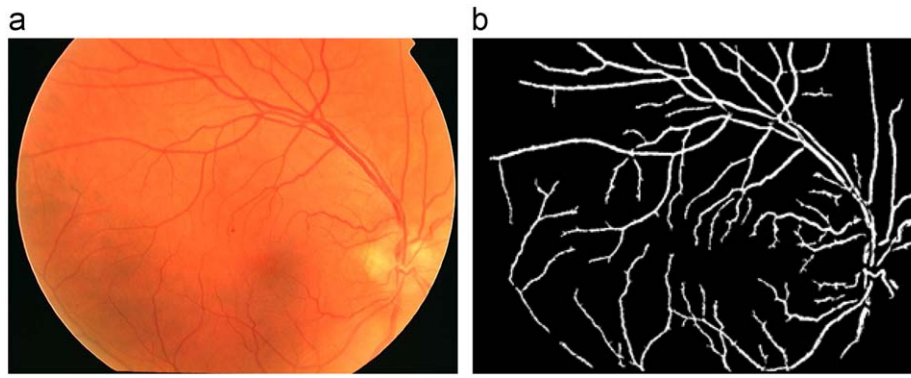
Fig. 9. The vascular map of a retinal image: (a) the sample image given in Fig. 1(b) and (b) the output of its vascular map.

Fig. 10. The remaining candidates from Fig. 8 after candidates on the blood vessels were removed.

Fig. 11. Result of region growing on the candidates in Fig. 10.

and maximum are the final detected microaneurysms. We applied this table to the candidates drawn from Fig. 11 and obtained the result in Fig. 14. The true candidates are then mapped back to the original image to show the location of true microaneurysms (inside the green squares, shown in Fig. 14(c)). As can be seen, a significant number of candidates have been removed (Fig. 14(b)). For the final output image given in Fig. 14(c), all true micro-aneurysms were detected with no false positives.
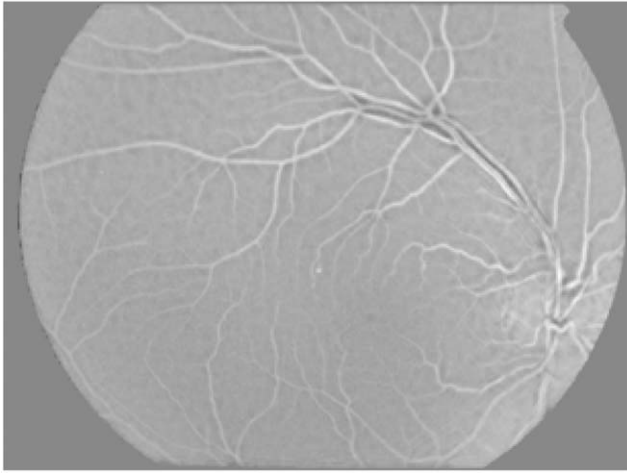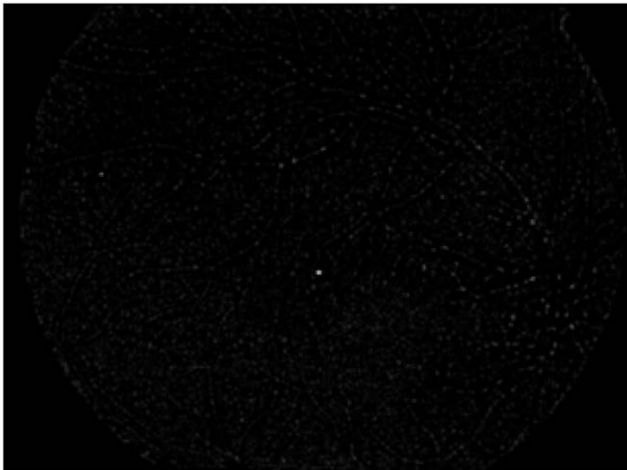
Table 1
The list of 31 features.

Feature number	Feature description
1	The area a of the candidate. Microaneurysms have a small area compared to other objects in the retina
2	The perimeter p of the candidate. Microaneurysms have a small perimeter compared to other objects in the retina
3	The aspect ratio $r = l/w$ where l and w are the major and minor axis lengths of the candidate. For a true microaneurysm its major and minor axes should be quite similar
4	The circularity $c = (4 \cdot \pi \cdot a)/p^2$. True microaneurysms are circular in shape
5	The total intensity i_{green} of the candidate in I_{green}. True microaneurysms have higher intensities
6	The total intensity i_{SC} of the candidate in I_{SC}
7	The average intensity of i_{green}, $m_{green} = i_{green}/a$
8	The average intensity of i_{SC}, $m_{SC} = i_{SC}/a$
9	The normalized intensity in I_{green}, $NI_{green} = (1/\sigma)(i_{green}-x)$ where σ and x are the standard deviation and mean pixel value of I_{bg}
10	The normalized intensity in I_{SC}, $NI_{SC} = (1/\sigma)(i_{SC}-x)$
11	The normalized average intensity in I_{green}, $NM_{green} = (1/\sigma)(m_{green}-x)$
12	The normalized average intensity in I_{SC}, $NM_{SC} = (1/\sigma)(m_{SC}-x)$
13	The intensity of $I_{darkest}$ in I_{match}
14	The compactness $v = \sqrt{\sum(d_i-d)^2/n}$ where d_i is the distance of each boundary pixel of the candidate to its center, d is the mean of all these distances and n is the number of boundary pixels. True microaneurysms are compact
15	The difference between the average pixel values of the candidate and a circular region (no including the candidate) centered on it in the red channel (RGB color space). The circular region is calculated by dilating the candidate with a disk of radius 6. Since microaneurysms have a Gaussian distribution when examining its grayscale values, the contrast of the microaneurysm with its background should be high
16–18	Repeat feature 15 but in the green channel, blue channel and hue channel from the HSI color space
19–22	The average Gaussian filter response of I_{green} with σ=1, 2, 4, and 8
23–26	The standard deviation response of I_{green} after Gaussian filtering with σ=1, 2, 4, and 8
27–29	The maximum, minimum and average correlation coefficient of the candidate. Candidates with a higher coefficient are more likely to be true microaneurysms
30	The major axis length of the candidate. Generally, microaneurysms do not have a significant major or minor axis length
31	The minor axis length of the candidate

4. Experimental results and analysis

The experimental results reported in this paper are mainly based on our work submitted to *retinopathy on-line challenge* (*ROC*),

Fig. 12. Sub-band image I_{SC} obtained by subtracting I_{bg} from I_{green}.
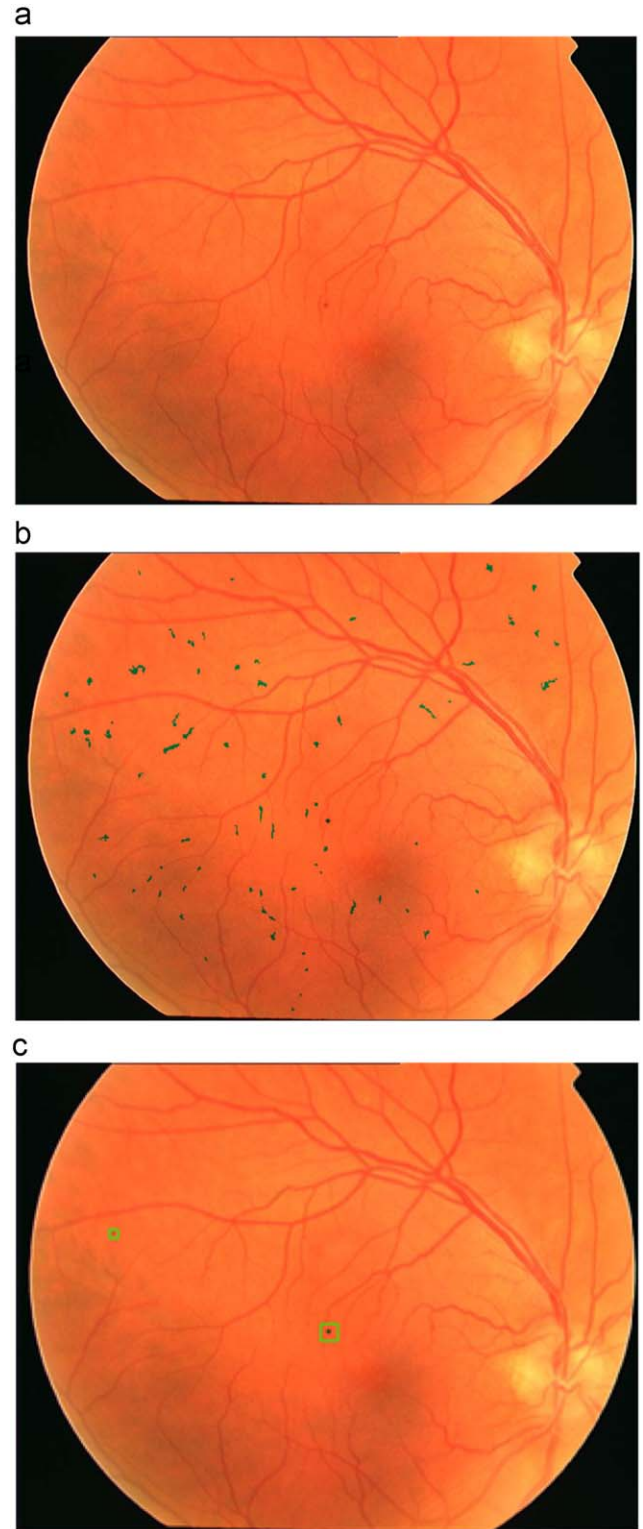

Fig. 13. Matched image I_{match} which shows possible lesions. This image was processed by removing vessels from Fig. 12 and enhancing its result with a Gaussian filter.

Table 2
The discrimination table of different retinal features.

Feature number	Min.	Max.	Feature number	Min.	Max.
1	2	109	17	−27.1471	6.368521
2	2	113.0122	18	−0.01944	0.002723
3	1	5.618986	19	27.66061	179.0988
4	0.090521	6.283185	20	0.01962	8.292589
5	58	10676	21	30.81245	180.773
6	338	19451	22	0.044188	6.747434
7	25.17241	177.0417	23	36.00843	182.7637
8	104.8125	221.9348	24	0.003416	3.00799
9	−0.31038	203.8908	25	37.95791	183.7483
10	6.138524	448.9355	26	0.009462	1.797795
11	−1.15234	0.921628	27	0.106603	0.785072
12	0.164831	5.08576	28	0	0.547187
13	7	255	29	0.053335	0.658546
14	0	3.743681	30	2.309401	29.53404
15	−31.368	2.863946	31	1.154701	14.09998
16	8	35.37533			

Fig. 14. The output of microaneurysm detection: (a) the original retinal image; (b) the output of coarse-level detection and (c) the final output of fine-level detection where the green squares mark the approximate location of the detected microaneurysms using the proposed algorithm. (For interpretation of the references to color in this figure legend, the reader is referred to the web version of this article.)

an international competition associated with *2009 SPIE medical imaging* (*MI*' 2009). The score of our submission was ranked second among all participants. The details of *ROC* competition are available on ROC website [22]. A preliminary performance evaluation was also conducted on the well established public dataset *DIARETDB1* (*standard diabetic retinopathy database*) [23,24]. The following

summarizes our testing results and comparison with other methods for performance evaluation.

A sequence of experiments was conducted on 100 images (split into 50 training and 50 test) in the public retinal image database provided on the ROC competition website [22]. The images were all taken with Topcon NW 100, NW 200 or Canon CR5-45NM "non-mydriatic" cameras at the default resolution and compression settings from patients with diabetes without known diabetic retinopathy (at the moment of photography). The images are a random sample of all patients that were noted to have "microaneurysms" from a large (> 10,000 patients) diabetic retinopathy screening program, and each image is from a different patient. All images are in JPEG compressed format with sizes 768×576, 1058×1061, 1062×1061, 1379×1383, 1381×1385, 1385×1382, 1386×1384, 1389×1383, 1389×1391 and 1394×1392 pixels. Each image comes with a reference standard that marks every microaneurysm agreed upon by the consensus of four experts. This reference standard helps to identify true microaneurysms used in the discrimination table. Some images contained so-called "do not care" objects where a consensus could not be reached or where the objects are not microaneurysms (e.g., hemorrhages, pigment spots, etc.). We applied the proposed algorithm on all images and did not consider or use the "do not care" objects. To segment the final response after applying the kernel functions we used threshold values ranging from 0.1 to 1.0, each time building a discrimination table according to the true microaneurysm feature values and using it to remove some candidates. We compared our algorithm with Math Morph [13], Waikato Retinal Imaging Group [22], Fujita Lab [22], LaTIM [22], IRIA-Group [22] and GIB Valladolid [22]. The algorithm described in [13] was implemented by ourselves and tested with the same data as the proposed algorithm. For [22] we referenced their published results (on the test dataset) since they used the ROC database as well. We were not able to compare the fusion algorithm in [13] because the reference standard provided did not label each pixel as required by this method.

The performance of our hierarchical approach based on MSCF for microaneurysms detection is evaluated by plotting sensitivity against the average number of false positives per image (FROC) using the 50 training images, shown in Fig. 15 as a dotted curve. Sensitivity is the number of true microaneurysms correctly detected while false positive is the number of non-microaneurysms detected as true microaneurysms. Please note that the horizontal axis is in logarithmic scale. The FROC plot also contains a solid curve, which is our implementation of Math Morph. As can be seen the majority of the dotted curve has a higher sensitivity compared with the solid curve for the same false positives per image. Table 3 lists the sensitivity of 1/8, 1/4, 1/2, 1, 2, 4 and 8 false positives per image of both methods derived from Fig. 15. In this table the proposed method has a greater sensitivity from 1/4 to 8 with the average of all seven points being 0.201 and 0.126 for Math Morph.

Fig. 16 illustrates the FROC plots of both MSCF and Math Morph after the coarse level. Table 4 lists the sensitivity (from this graph) using the same false positives as Table 3. Even though the sensitivity for 1/8, 1/4, 1/2 and 1 false positives per image are not available, it can be inferred from 2, 4 and 8 false positives per image that the missing values will be lower than that those in Table 3. This shows the benefit of the second level in removing false candidates.

Results based on the 50 test images are displayed in Fig. 17, also in the form of a FROC plot. Again, the dotted line represents MSCF while the solid line is Math Morph. The same trend found in Fig. 15 applies to Fig. 17 where the majority of MSCF points are higher than Math Morph. Table 5 which measures the same false positives per image as Table 3 except for the test data with the addition of Waikato Retinal Imaging Group, Fujita Lab, LaTIM, IRIA-Group and GIB Valladolid supports the previous claim, as the sensitivity of MSCF is greater than Math Morph, Waikato Retinal Imaging Group, Fujita Lab, IRIA-Group, GIB Valladolid and is slightly worse than LaTIM. The average sensitivity being 0.206—Waikato Retinal Imaging Group, 0.310—Fujita Lab, 0.381—LaTIM, 0.357—MSCF, 0.189—IRIA-Group, 0.322—GIB Valladolid and 0.087—Math Morph. The remaining true microaneurysms not detected were due to the quality of the images, the selection of sigma for the Gaussian filter, the location of the microaneurysms being too close to blood vessels and little contrast between the microaneurysm and its surrounding background.

The experiments raise four particular issues which require further consideration. First, there is the quality of the images, which are JPEG compressed and therefore some of the microaneurysms too small or too blurred to be seen with the naked eye. Second there is the choice of scales for the Gaussian kernel. The use of only small scales means that larger microaneurysms will not be extracted because the smaller kernel cannot cover/match the larger spots and thereby produces a lower correlation

Table 3
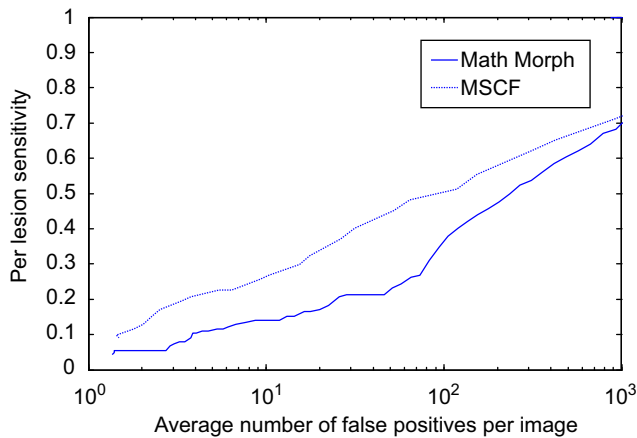The average number of false positives per image for training data.

FPs/scan	1/8	1/4	1/2	1	2	4	8	Average
MSCF	**0.060**	**0.096**	**0.138**	**0.189**	**0.267**	**0.311**	**0.345**	**0.201**
Math Morph	0.081	0.087	0.107	0.107	0.141	0.166	0.196	0.126
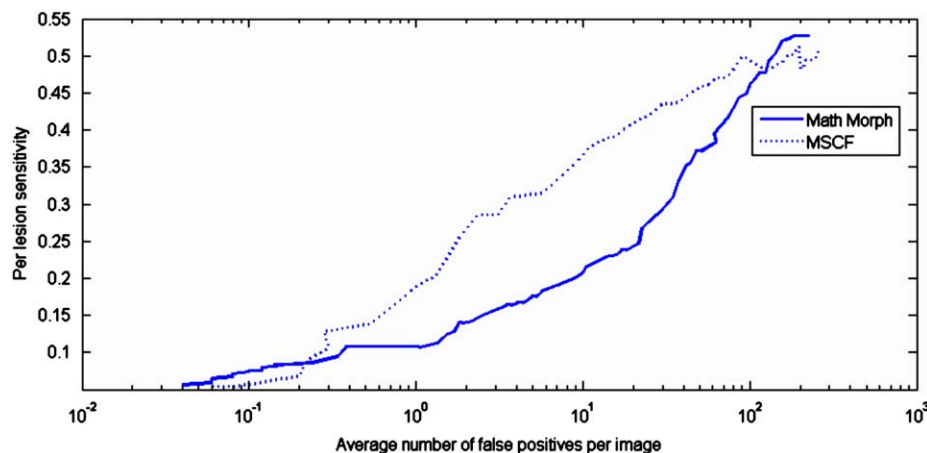
Fig. 15. Plot of FROC comparing MSCF (dotted curve) with Math Morph (solid curve) on the training data.

coefficient. The same problem arises when using a larger scale to cover/match a small microaneurysm. If such candidate micro-aneurysms are not detected after the coarse level they will be lost forever. Third, a few microaneurysms located next to or nearby blood vessels are removed in the coarse level. This is because these microaneurysms are recognized as part of the vascular map and therefore are removed along with real vessels. Fig. 18 below illustrates this problem where Fig. 18(a) is a cropped color retinal image with marked (green squares) microaneurysms Fig. 18(b) shows candidates detected from Fig. 18(a) and (c) is the vascular map of Fig. 18(a). The central microaneurysm (enclosed in dashes) in Fig. 18(a) is detected as seen in Fig. 18(b) but also appears as a vessel in Fig. 18(c). This subsequently removes it as a candidate from Fig. 18(b) in the next step of the coarse level. We will attempt to resolve this problem as part of the future work.

A fourth issue for further consideration relates to the effect of contrast on true and false detected microaneurysms. When true microaneurysms have a low contrast with its background, as can be seen in the examples in Fig. 19, the microaneurysms will not exhibit a Gaussian shape and it becomes difficult for the Gaussian kernels to produce a high correlation coefficient (see Table 6). From our results several of the spots detected as false microaneurysms are circular in shape and have significant contrast with its background which explains its high correlation coefficient. Of these, some are possibly microaneurysms (where a consensus was not reached by the 4 experts). Fig. 20 shows four examples of these contentious spots with Table 7 displaying their correlation coefficients. We deem these objects reasonable to be detected as they resemble true microaneurysms.

The performance evaluation of our proposed method was further conducted on another well established public database DIARETDB1 [23, 24]. DIARETDB1 offers a general platform and a powerful testing toolkit with 89 images taken under a common imaging protocol to benchmark diabetic retinopathy detection

Fig. 16. Plot of FROC comparing MSCF (dotted curve) with Math Morph (solid curve) after the coarse level on the training data.
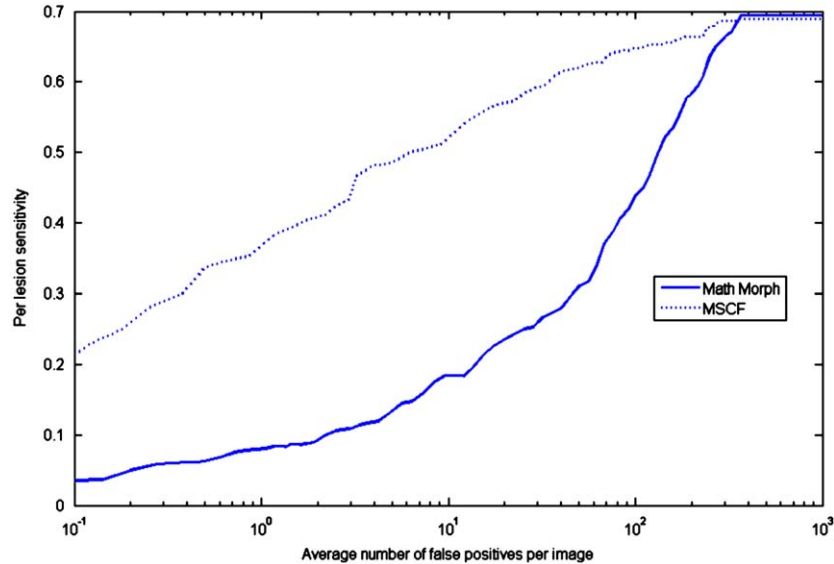
Table 4
The average number of false positives per image after the coarse level for training data.

FPs/scan	1/8	1/4	1/2	1	2	4	8	Average
MSCF	N/A	N/A	N/A	N/A	**0.126**	**0.210**	**0.243**	**0.193**
Math Morph	N/A	N/A	N/A	N/A	0.055	0.104	0.136	0.098

Fig. 17. Plot of FROC comparing MSCF (dotted curve) with Math Morph (solid curve) on the test data.

Table 5
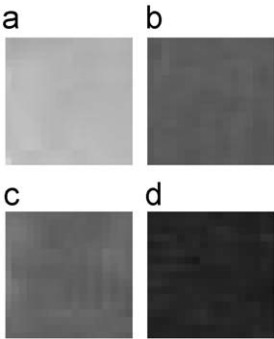The average number of false positives per image for test data.

FPs/scan	1/8	1/4	1/2	1	2	4	8	Average
Waikato Retinal Imaging Group	0.055	0.111	0.184	0.213	0.251	0.300	0.329	0.206
Fujita Lab	0.181	0.224	0.259	0.289	0.347	0.402	0.466	0.310
LaTIM	0.166	0.230	0.318	0.385	0.434	0.534	0.598	0.381
MSCF	**0.198**	**0.265**	**0.315**	**0.356**	**0.394**	**0.466**	**0.501**	**0.357**
IRIA-Group	0.054	0.085	0.117	0.169	0.230	0.289	0.379	0.189
GIB Valladolid	0.190	0.216	0.254	0.300	0.364	0.411	0.519	0.322
Math Morph	0.035	0.055	0.063	0.080	0.092	0.118	0.168	0.087
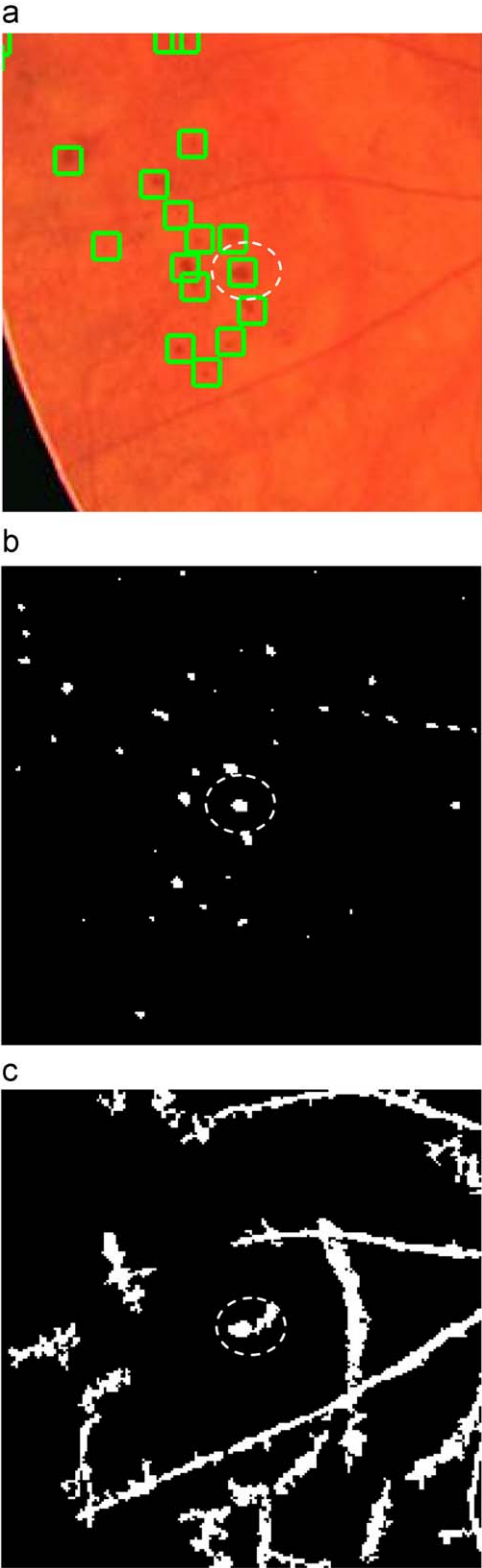
Fig. 18. True microaneurysm being recognized as part of the blood vessel: (a) a cropped retinal image marked with true microaneurysms; (b) candidates microaneurysms detected in (a), (c) vascular map of (a). The central microaneurysm enclosed with dashes in (a) and (b) is detected as part of the blood vessel in (c).
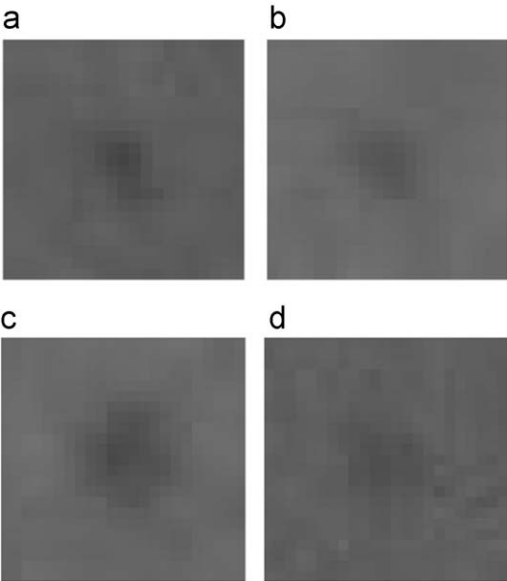

Fig. 19. True microaneurysms with low contrast.

Table 6
True lesions with low intensity contrast.

True lesion	Max. response
Fig. 19(a)	0.1696
Fig. 19(b)	0.1624
Fig. 19(c)	0.1934
Fig. 19(d)	0.1715

Fig. 20. False positive microaneurysm candidates with high contrast.

Table 7
Examples of false positive candidates that resemble true lesions.

False lesion	Max. response
Fig. 20(a)	0.7527
Fig. 20(b)	0.7235
Fig. 20(c)	0.6564
Fig. 20(d)	0.6269

methods, where image samples are 1500×1152 pixels in size and were collected at Kuopio University Hospital with the same $50°$ FOV digital camera. Independent markings of any possible microaneurysms by medical experts on the ground truth images are also provided for cross referencing and assessment. The performance comparison between our MSCF approach and Math Morph algorithm [13] on DIARETDB1 is represented by FROC plots and sensitivity measurement. Our preliminary results are displayed in Fig. 21 and further summarized in Table 8. A total number of 11 images are randomly selected from both the test
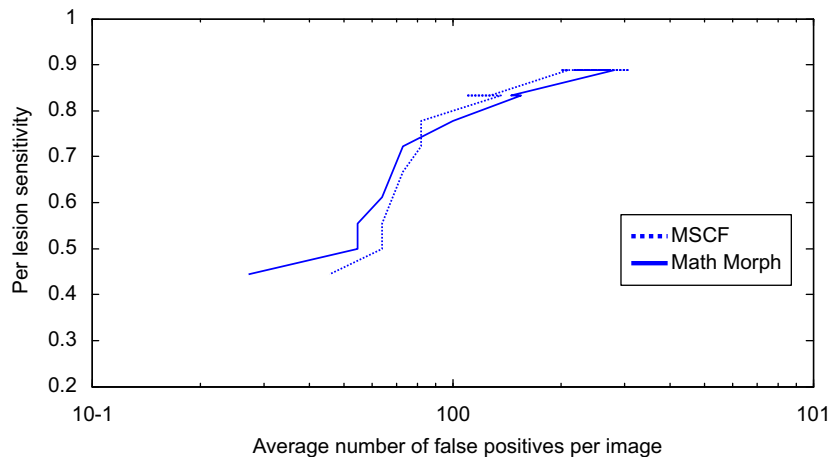
Fig. 21. Plot of FROC comparing MSCF (dotted curve) with Math Morph (solid curve), preliminary results on DIARETDB1.

Table 8
The average number of false positives per image for DIARETDB1 (preliminary results).

FPs/scan	1/8	1/4	1/2	1	2	4	8	Average
MSCF	N/A	N/A	0.458	0.796	0.886	N/A	N/A	0.713
Math Morph	N/A	N/A	0.491	0.778	0.856	N/A	N/A	0.708

and training set of DIARETCB1 in the experiment, where 6 images were from the training set and 5 images from the test set. These 11 images were used in both training our proposed algorithm and testing it. For the ground truth a confidence level of 75 was used in accordance with guidelines set by DIARETDB1. Fig. 21 plots the FROC of MSCF and Math Morph using the 11 images from DIARETDB1. Table 8 shows the sensitivity and false positives per image of Fig. 21, where the proposed MSCF has a higher sensitivity of average value 0.713 compared with the average sensitivity value 0.708 by Math Morph algorithm. It is noted that the FROC plots on DIARETDB1 are not as smooth as what are obtained on ROC dataset. The reason is that only a small number of 11 images was used for DIARETDB1 while the number of 50 training images was involved in ROC. As a result, the total number of true microaneurysms on DIARETDB1 will be far less compared to the number obtained on 50 ROC (training) images. In addition, since the quality of DIARETDB1 images is higher than ROC images, microaneurysms on DIARETDB1 are better detected evident by the higher sensitivity and lower false positive (see Table 8).

It is also noted that there is a significant difference in performances of our proposed MSCF method on different dataset—DIARETDB1 and ROC. In fact, such a difference truly reflects the purpose and focus of these two popular public datasets. DIARETDB1 aims to offer a general platform and a powerful testing toolkit under a common imaging protocol to benchmark diabetic retinopathy detection method, which contains images captured using a single device and unified image format for its immediate clinical application to computer aided mass DR screening. On the other hand, ROC is concerned with the international competition by ranking the performance of different approaches to difficult cases, where ROC images were captured with various devices under different conditions. Since images in DIARETDB1 are uncompressed compared to ROC, microaneurysms are visually clearer and better presented in the image data. Therefore, the detection result on DIARETDB1 is much better than on ROC. Since our proposed method is based on matching multi-scale Gaussian kernels defined beforehand irrespective of image quality and resolution, we did not

customize or tune any parameters to achieve the improvement. The performance of MSCF and Math Morph on DIARETDB1 is similar because DIARETDB1 images are of a higher quality with clearly visible microaneurysms for easy detection. However, the robustness of our proposed MSCF method can be further demonstrated by the significant performance improvement of higher sensitivity compared with Math Morph to deal with images of poor quality and diverse formats on ROC dataset.

5. Conclusion and future work

In this paper we proposed a hierarchical approach based on multi-scale correlation filtering (MSCF) to detect all microaneurysms from a color retinal image. This consisted of coarse level: microaneurysm candidate detection using MSCF and fine level: true microaneurysm classification. The approach was evaluated extensively using the public retinal image database provided on the ROC competition website [22] as part of our participation in this event. We conclude that the proposed approach is effective and efficient for intensity-based microaneurysm detection and localization for DR diagnosis. The selection of scales in the first level is vital to the success of succeeding steps. Sigma values have to be chosen such that the kernel can match microaneurysm of various sizes always producing a high correlation coefficient. Currently only five scales are used. If more scales specifically designed to match small and large microaneurysms are implemented and then combined to form a scale production, this might improve the existing results to deal with the general detection of microaneurysms. Further improvement of the proposed algorithm is to develop an automatic scale selection scheme which can determine the best scale for the system based on the training set.

It is noted that DIARETDB1 [24] is a well established public dataset which consists of more images (89) than the number of test images offered by ROC website (50). More importantly, images in DIARETDB1 database were acquired in the same environment, which provides a general platform to benchmark different algorithms for the detection of microaneurysms. It will be helpful to evaluate all of the ROC algorithms against DIARETDB1 for a better benchmarking standard. We plan to collaborate with different research groups and undergo a comprehensive performance evaluation of different algorithms on DIARETDB1 with the consent of the researchers concerned in the future. In addition, we will also compare the performance of our discrimination table against k-NN classifier on DIARETDB1 to provide more experimental insight of their discrimination power as part of the general

benchmarking. Currently we are working on a new wavelet-based Gaussian mixture model to reduce the feature set for discrimination without training process. We will compare this new method with other existing algorithms including the classifier based approach and present our findings in another research paper.

Acknowledgments

References

[1] M. Goldbaum, S. Moezzi, A. Taylor, S. Chatterjee, J. Boyd, E. Hunter, R. Jain, Automated diagnosis and image understanding with object extraction, object classification, and inferencing in retinal images, in: Proceedings of the IEEE International Conference on Image Processing, vol. 3, 1996, pp. 695–698.

[2] M. Cree, J. Olson, K. McHardy, P. Sharp, J. Forrester, A fully automated comparative microaneurysm digital detection system, Eye 11 (1997) 622–628.

[3] J. Hipwell, F. Strachant, J. Olson, K. McHardy, P. Sharp, J. Forrester, Automated detection of microaneurysms in digital red-free photographs: a diabetic retinopathy screening tool, Diabetic Med. 17 (2000) 588–594.

[4] M. Larsen, J. Godt, N. Larsen, H. Lund-Andersen, A. Sjølie, E. Agardh, H. Kalm, M. Grunkin, D. Owens, Automated detection of fundus photographic red lesions in diabetic retinopathy, Invest. Ophthalmol. Vis. Sci. 44 (2003) 761–766.

[5] T. Walter, J.C. Klein, P. Massin, A. Erginay, A contribution of image processing to the diagnosis of diabetic retinopathy—detection of exudates in color fundus images of the human retina, IEEE Trans. Med. Imaging 21 (2002) 1236–1243.

[6] C. Sinthanayothin, J.F. Boyce, T.H. Williamson, H.L. Cook, E. Mensah, S. Lal, D. Usher, Automated detection of diabetic retinopathy on digital fundus images, Diabetic Med. 19 (2002) 105–112.

[7] A.J. Frame, P.E. Undill, M.J. Cree, J.A. Olson, K.C. McHardy, P.F. Sharp, J.F. Forrester, A comparison of computer based classification methods applied to the detection of microaneurysms in opthalmic fluorescein angiograms, Comput. Biomed. Res. 28 (1998) 225–238.

[8] A.M. Mendonca, A.J. Campilho, J.M. Nunes, Automatic segmentation of microaneurysms in retinal angiograms of diabetic patients, Proc. IEEE Int. Conf. Image Anal. Appl. (1996) 728–733.

[9] T. Spencer, R.P. Phillips, P.F. Sharp, J.V. Forrester, Automated detection and quantification of microaneurysms in fluorescein angiograms, Graefe's Arch. Clin. Exp. Ophthalmol. 230 (1991) 36–41.

[10] C. Sinthanayothin, V. Kongbunkiat, S. Phoojaruenchanachai, A. Singalavanija, Automated screening system for diabetic retinopathy, in: Proceedings of the IEEE Image and Signal Processing and Analysis, 2003, pp. 915–920.

[11] G.G. Gardner, D. Keating, T.H. Williamson, A.T. Elliott, Automatic detection of diabetic retinopathy using an artificial neural network: a screening tool, Br. J. Ophthalmol. 80 (1996) 940–944.

[12] K. Estabridis, R.J.P. de Figueiredo, Automatic detection and diagnosis of diabetic retinopathy, in: Proceedings of the IEEE International Conference on Image Processing, 2007, pp. 445–448.

[13] M. Niemeijer, B. van Ginneken, J. Staal, M.S.A. Suttorp-Schulten, M.D. Abramoff, Automatic detection of red lesions in digital color fundus photographs, IEEE Trans. Med. Imaging 24 (2005) 584–592.

[14] T. Spencer, J.A. Olson, K.C. McHardy, P.F. Sharp, J.V. Forrester, An image-processing strategy for the segmentation of microaneurysms in fluorescein angiograms of the ocular fundus, Comput. Biomed. Res. 29 (1996) 284–302.

[15] H. Leung, J.J. Wang, E. Rochtchina, T.Y. Wong, R. Klein, P. Mitchell, Impact of current and past blood pressure on retinal arteriolar diameter in older population, J. Hypertens. (2003) 1543–1549.

[16] P. Mitchell, H. Leung, J.J. Wang, E. Rochtchina, A.J. Lee, T.Y. Wong, R. Klein, Retinal vessel diameter and open-angle glaucoma: the Blue Mountains eye study, Ophthalmology (2005) 245–250.

[17] R. Chrástek, M. Wolf, K. Donath, H. Niemann, D. Paulus, T. Hothorn, B. Lausen, L. Lämmer, C.Y. Mardin, G. Michelson, Automated segmentation of the optic nerve head for diagnosis of glaucoma, IEEE Trans. Med. Image Anal. 9 (2005) 297–314.

[18] J.J. Wang, B. Taylor, T.Y. Wong, B. Chua, E. Rochtchina, R. Klein, P. Mitchell, Retinal vessel diameters and obesity: a population-based study in older persons, Obes. Res. (2006) 206–214.

[19] H.R. Taylor, J.E. Keeffe, World blindness: a 21st century perspective, Br. J. Ophthalmol. 85 (2001) 261–266.

[20] R. Klein, S.M. Meuer, S.E. Moss, B.E. Klein, Retinal microaneurysm counts and 10-year progression of diabetic retinopathy, Arch. Ophthalmol. 113 (1995) 1386–1391.

[21] J. Domingo, G. Ayala, A. Sim, E. de Ves, L. Martlnez-Costa, P. Marco, Irregular motion recovery in fluorescein angiograms, Pattern Recognition Lett. 18 (1997) 805–821.

[22] Retinopathy Online Challenge, ⟨http://roc.healthcare.uiowa.edu/⟩.

[23] T. Kauppi, V. Kalesnykiene, J.K. Kamaraniene, L. Lensu, I. Sorri, A. Raninen, R. Voutilainen, H. Uusitalo, H. Kalviainen, J. Pietil, The DIARETDB1 diabetic retinopathy database and evaluation protocol, in: Proceedings of the British Machine Vision Conference, 2007, pp. 252–261.

[24] DIARETDB1—Standard Diabetic Retinopathy Database, ⟨http://www.it.lut.fi/project/imageret/diaretdb1/⟩.

[25] K. Huang, M. Yan, A local adaptive algorithm for microaneurysms detection in digital fundus images, in: Proceedings of Computer Vision for Biomedical Image Applications, 2005, pp. 103–113.

[26] A.D. Fleming, S. Philip, K.A. Goatman, J.A. Olson, P.F. Sharp, Automated microaneurysm detection using local contrast normalization and local vessel detection, IEEE Trans. Med. Imaging (2006) 1223–1232.

[27] T. Walter, P. Massin, A. Erginay, R. Ordonez, C. Jeulin, J.C. Klein, Automatic detection of microaneurysms in color fundus images, Med. Image Anal. (2007) 555–566.

[28] M. Lamard, G. Quellec, P.M. Josselin, G. Cazuguel, B. Cochener, C. Roux, Detection of lesions in retina photographs based on the wavelet transform, in: Proceedings of the International Conference of the IEEE Engineering in Medicine and Biology Society, 2006, pp. 2435–2438.

[29] L. Zhang, Q. Li, J. You, D. Zhang, Modified matched filter with double-side thresholding and its application to proliferative diabetic retinopathy screening, IEEE Trans. Inf. Technol. Biomed. (2009) 528–534.

About the Author—BOB ZHANG graduated from York University with B.Sc. in Computer Science in 2005 and obtained his M.Sc. from Concordia University, Canada in 2007. Currently he is a Ph.D. candidate in Department of Electrical and Computer Engineering, the University of Waterloo, Canada. His research interest includes pattern recognition, medical imaging and machine learning.

About the Author—XIANGQIAN WU graduated from Harbin Institute of Technology (HIT), China with M.Sc. and Ph.D. in 2000 and 2004, respectively. Currently he is an associate professor in HIT with research interests in image processing and pattern recognition.

About the Author—JANE YOU obtained her B.Eng. in Electronic Engineering from Xi'an Jiaotong University in 1986 and Ph.D. in Computer Science from La Trobe University, Australia in 1992. She was a lecturer at the University of South Australia and senior lecturer at Griffith University from 1993 till 2002. Currently she is an associate professor at the Hong Kong Polytechnic University. Her research interests include image processing, pattern recognition, medical imaging, biometrics computing, multimedia systems and data mining.

About the Author—QIN LI graduated from Zhengzhou University with B.Sc. in Computer Science and obtained his M.Sc. in Computer Science from the University of Newcastle, UK. Currently he is a Ph.D. candidate at the Hong Kong Polytechnic University. His research area includes image processing, pattern recognition and multimedia systems.

About the Author—FAKHRI KARRAY is a professor in Department of Electrical and Computer Engineering, the University of Waterloo, Canada. His research interests include machine learning, data mining, computer systems.